

Enhanced Structural Stability of Sb_2Se_3 via Pressure-Induced Alloying and AmorphizationHPSTAR
908-2020Hu Cheng,[∇] Junran Zhang,[∇] Pengfei Yu, Chao Gu, Xiangting Ren, Chuanlong Lin,^{*} Xiaodong Li, Yusheng Zhao, Shanmin Wang,^{*} and Yanchun Li^{*}Cite This: *J. Phys. Chem. C* 2020, 124, 3421–3428

Read Online

ACCESS |



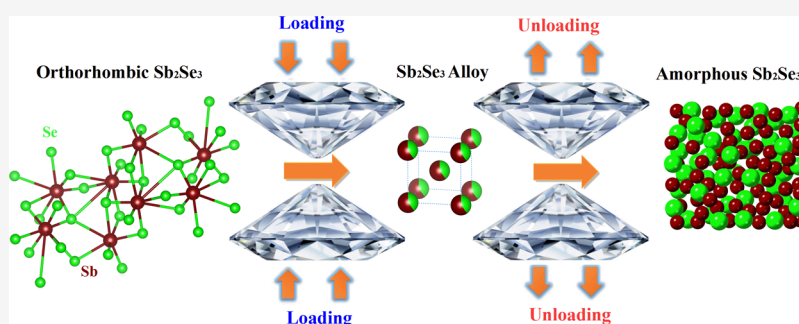
Metrics & More



Article Recommendations



Supporting Information



ABSTRACT: In this work, we revealed that Sb_2Se_3 has one second-order isostructural phase transitions before it eventually transformed into a site-disordered alloy during compression. Then, a rare amorphization of alloy was discovered with decreasing pressure in Sb_2Se_3 by performing in situ high-pressure X-ray diffraction (XRD) and Raman experiments, which may be owed to the significant difference in atomic electronegativity of Sb_2Se_3 . Compared to the original structure, the amorphous phase of Sb_2Se_3 is more stable at high pressure. Surprisingly, the structural stability of amorphous Sb_2Se_3 at varying temperatures was also significantly improved via recompression. Our findings will provide insight into the formation mechanism of the bcc alloys and amorphization in A_2B_3 ($\text{A} = \text{Sb}, \text{Bi}$; $\text{B} = \text{S}, \text{Se}, \text{Te}$) compounds and, especially, offer a new way to prepare amorphous materials.

INTRODUCTION

Generally, amorphous materials can be obtained by rapid solidification of vapors and the melts,^{1–3} which have been recognized and widely employed in the field of material science. In addition, several alternative routes have been constructed, such as gas absorption of metal alloys,^{4–6} mechanical alloying,^{7,8} anomalous diffusion,⁹ or pulsed laser irradiation,¹⁰ etc. Compared to these traditional methods, pressure-induced amorphization is more complex and unique and has been observed in various elements,^{11–15} compounds,^{16–22} and alloys.^{23–25} However, almost all of these transformations are found in the compression process, so far widely unknown to the crystalline-to-amorphous transition with releasing pressure. Here, we find that a Sb–Se amorphous phase can be synthesized by pressurizing and depressurizing Sb_2Se_3 .

As typical A_2B_3 -form ($\text{A} = \text{Sb}, \text{Bi}$; $\text{B} = \text{S}, \text{Se}, \text{Te}$) compounds, Sb_2Se_3 has attracted a lot of interest due to the interesting properties for several applications, such as thermoelectric devices,²⁶ solar cells,²⁷ optical recording material,²⁸ and hydrogen storage materials,²⁹ etc. In recent years, Bi_2Te_3 , Sb_2Te_3 , and Bi_2Se_3 have been experimentally observed as the simplest 3D topological insulators,^{30,31} which make A_2B_3 became a hot topic in the field of material research. External

pressure can be used to tune the electronic and atomic structures of materials. It has been verified that the thermoelectric properties of Bi_2Te_3 , Bi_2Se_3 , and Sb_2Te_3 can be improved under high pressures.^{32–35} Also, pressure-induced electronic topological transitions (ETTs),^{36–40} superconductivity,^{41–47} and metallization transitions^{48–50} of these compounds have also been extensively investigated. However, compared to the sufficient high-pressure studies of rhombohedral forms of A_2B_3 (Bi_2Te_3 , Sb_2Te_3 , and Bi_2Se_3),^{39,45,51–59} the $Pnma$ types of A_2B_3 (Bi_2S_3 , Sb_2S_3 , and Sb_2Se_3) have not received similar attention because of the lack of topological properties, and their structural transformations at high pressure are still indistinct. By a combination of high-pressure XRD and Raman measurements, Efthimiopoulos et al. found that the $Pnma$ phase of Bi_2S_3 could persist up to 50 GPa, further compression leads to structural disorder.⁴⁰ Subsequently, two pressure-induced phase transitions were reported in Sb_2S_3 ,⁶⁰ and an amorphous state was observed after full decompression

Received: December 12, 2019

Revised: January 15, 2020

Published: January 17, 2020



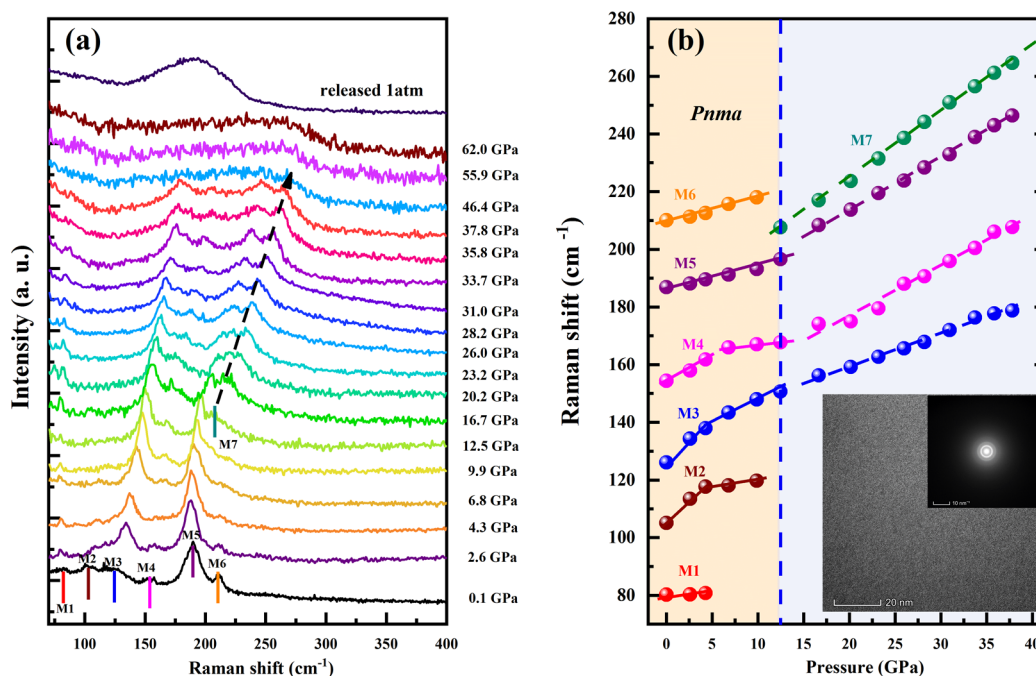


Figure 1. (a) Raman spectra of Sb_2Se_3 vs pressure during compression and decompression at room temperature with neon as the PTM, the excitation wavelength was 532 nm. (b) Pressure dependence of Raman mode frequencies for Sb_2Se_3 , the inset shows the HRTEM images of fully released Sb_2Se_3 obtained from Raman experiment.

from 53 GPa with helium as pressure-transmitting media (PTM). Whereas, more recently, based on the high-pressure Raman spectra studies, Dai et al. suggested that these transitions in Sb_2S_3 were reversible under hydrostatic condition,⁵⁰ while an amorphization occurred under a nonhydrostatic condition. Nevertheless, few work focuses on the decompression process in A_2B_3 compounds, the formation mechanism of these amorphizations is still not clear. In the case of Sb_2Se_3 , the phase evolution paths of this A_2B_3 -form material are even more uncertain due to the negligence of the laser heating effect on the samples in the compression process and the absence of the details on the decompression.⁶¹

In the present work, we systematically investigated the pressure-induced structural transitions of Sb_2Se_3 in the compression and decompression process with the combination of high-resolution synchrotron XRD, Raman spectroscopy, resistance measurement, and high-resolution transmission electron microscopy (HRTEM). We have detected two phase transitions at about 12.4 and 52.2 GPa with increasing pressure, and the results are different from previous work. Then, a PTM-independence amorphous phase appeared with decreasing pressure. We attribute the amorphization to the differences in atomic electronegativity. More importantly, the amorphous Sb_2Se_3 is more stable at high pressure, and its structural stability could also be enhanced by recompressing. Our results can be applied to other A_2B_3 materials and other similar structural evolutions under high pressure.

EXPERIMENTAL PROCEDURES

High-Pressure XRD Experiments. Several high-pressure angle-dispersive XRD experiments were performed in a symmetric diamond anvil cell (DAC) with a pair of diamond anvils with a culet diameter of 300 μm . Commercially available Sb_2Se_3 powder (Alfa Aesar, 99.999%) was pressed into a thin slice and then placed in a 110 μm -diameter hole in a

preindented T301 gasket with 35 μm thickness. Neon, methanol–ethanol (4:1) mixture, and NaCl powder were used as the PTM in the first, second, and third runs, respectively. As an important supplement, two independent runs are also performed with different experimental pressure ranges with a methanol–ethanol (4:1) mixture as the PTM (runs 4 and 5). Pressure was determined by ruby fluorescence.⁶² Run 1 was conducted at the 16BM-D beamline of the high-pressure collaborative access team with $\lambda = 0.2592$ \AA , at APS-ANL. Runs 2–6 were conducted at the 4 W2 beamline of the Beijing Synchrotron Radiation Facility (BSRF) with $\lambda = 0.6199$ \AA . The powder diffraction patterns were collected with a Mar345 (run 1) or Pilatus (runs 2–5) image plate and integrated with the FIT2D software package.⁶³ The diffraction data were analyzed with GSAS+EXPGUI program.⁶⁴

High-Pressure Raman Experiments. The sample was loaded into a hole of 120 μm diameter in a T301 gasket and compressed between two 300 μm culet diamond anvils. Neon was used as the PTM. Pressure was determined by ruby fluorescence.⁶² The Raman spectra were collected at room temperature with a commercial SENTERRA (Bruker) confocal laser micro-Raman spectrometer using a 532 nm excitation laser with a spectra resolution about 1.5 cm^{-1} . To avoid the oxidation of Sb_2Se_3 at varying temperatures, below about 3 GPa, the laser power is set at 0.25 mW, and the exposure time is 240 s. Further compression and below about 15 GPa, the laser power should be less 12.5 mW, and the exposure time is 300 s. Above that pressure, the laser power is set at 12.5 mW, and the exposure time is 200 s.

High-Pressure Electrical Resistance Measurements. The pressure dependence of electrical resistance for Sb_2Se_3 was measured by using the standard four electrode method in a DAC with the anvil culet of 300 μm in diameter. Pressure in the chamber was determined by the ruby fluorescence

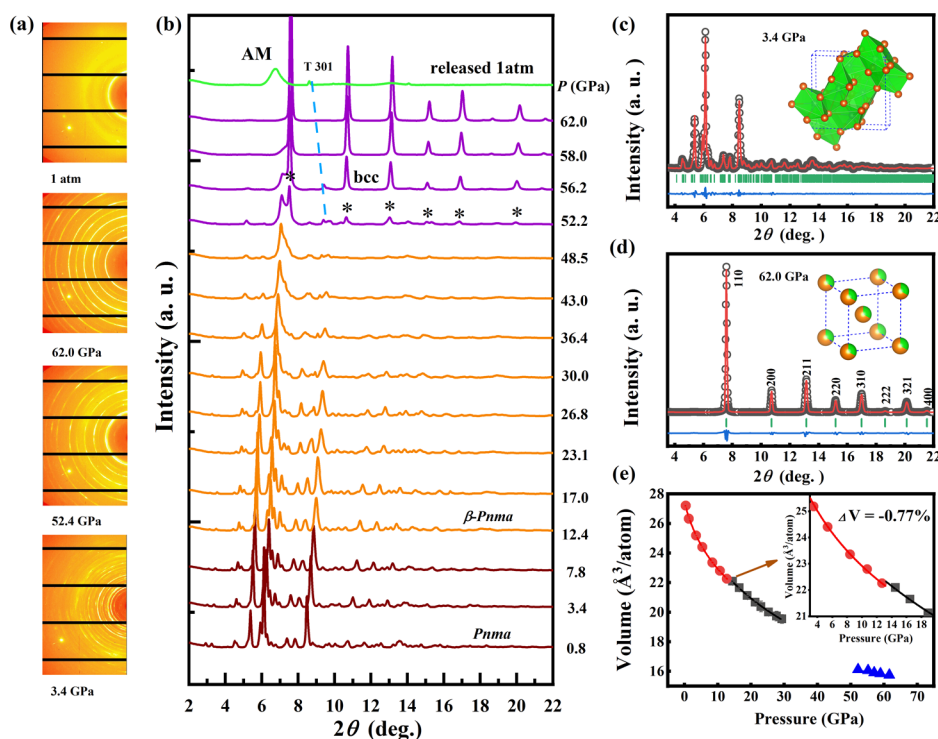


Figure 2. Structural evolutions of Sb_2Se_3 obtained during compression up to 62.0 GPa (run 1a) and decompression: (a) the raw 2D XRD patterns and (b) integrated XRD 1D profiles (asterisks: the new peaks of the bcc phase); (c) refinement of the 3.4 GPa XRD data obtained from run 1a with orthorhombic space group $Pnma$ from which we obtained the lattice parameters $a = 11.772(1)$ Å, $b = 3.9752(4)$ Å, and $c = 11.625(1)$ Å; (d) refinement of the 62.0 GPa XRD data obtained from run 1a with cubic space group $Im\bar{3}m$ from which we obtained the lattice parameters $a = 3.134(2)$ Å; (e) the pressure dependence of unit cell volume per atom for the three phases of Sb_2Se_3 (the solid lines represent the fitted Birch–Murnaghan EOS⁷¹ functions to the measured P – V data, with B_0' fixed as 4, the ambient pressure isothermal bulk modulus B_0 is estimated as 36(3), 44(2), and 200(19) GPa for the $Pnma$, β - $Pnma$, and bcc phases, respectively). The inset shows the details of the unit cell volume of the $Pnma$ and β - $Pnma$ phases as a function of pressure).

method.⁶² Fine cubic boron nitride (cBN) powder was used to cover the gasket as an insulating layer. No PTM was loaded to avoid additional errors in the electrical measurements.

Transmission Electron Microscopy (TEM). To verify the amorphization of Sb_2Se_3 obtained from the Raman experiments, we conducted TEM studies on the quenched sample. The TEM observations were performed at 200 kV in a Talos F200X microscope equipped with an energy-dispersive X-ray (EDX) spectrometer.

As a contrast, high-pressure XRD and Raman scattering measurements of Bi_2Te_3 and Sb_2Te_3 were performed without PTM.

RESULTS AND DISCUSSION

Given that Raman spectroscopy is a more sensitive probe for isostructural transitions and to better understand the high-pressure behavior of Sb_2Se_3 , high-pressure Raman experiments were carried out on Sb_2Se_3 at room temperature with neon as PTM. We can resolve six modes in our Raman spectra, marked as M1 (80.2 cm^{-1}), M2 (105.1 cm^{-1}), M3 (126 cm^{-1}), M4 (154.4 cm^{-1}), M5 (186.9 cm^{-1}), and M6 (210.0 cm^{-1}) at ambient pressure, as shown in Figure 1a, which is very different from the reported literatures^{61,65} but is consistent with the more recent study performed by Shongalova et al.⁶⁶ M1–M3 are very weak and broad, which may lead to the absence of them in Bera's work.⁶⁵ On the other hand, the Raman spectra of Sb_2Se_3 show a pronounced dependence on the laser heating at low pressure, which has been confirmed by Shongalova et al.⁶⁶ and this work (Figure S1). Hence, we attribute the Raman

peaks observed in Efthimiopoulos's work at 1 bar to the cubic Sb_2O_3 rather than orthorhombic Sb_2Se_3 .

Upon compression, these modes of Sb_2Se_3 shift to higher values. A large increase in the intensity of M3 within a narrow pressure range of 0–2.6 GPa is observed in Figure 1a, both M5 and M6 increase linearly up to 12.5 GPa, as shown in Figure 1b, while the pressure slopes of three other modes (M2, M3, and M4) reduce at 4.3 GPa. With increasing pressure, the weak M1 will disappear at 6.8 GPa, and neither M2 nor M6 can be observed above 9.9 GPa. As pressure was increased to 12.5 GPa, a new mode M7 appeared with frequency increasing linearly up to 37.8 GPa, and M3, M4, and M5 also show a slope change at 12.5 GPa, which means that a new phase transition has occurred. When the pressure was further increased to 41.1 GPa, the Raman spectra become rather featureless. Upon releasing pressure from 62.0 GPa, Sb_2Se_3 transformed into an amorphous state and marked with a very broad mode, as shown in Figure 1a. The HRTEM images further revealed that Sb_2Se_3 transformed to AM after releasing pressure, as shown in Figure 1b.

To further explore the structural properties of Sb_2Se_3 under pressure, high-pressure XRD experiments were performed. The selected XRD patterns of Sb_2Se_3 measured at various pressures during compression and decompression with neon as PTM (run 1a) at room temperature are shown in Figure 2a,b. Under ambient conditions, all diffraction peaks of Sb_2Se_3 could be indexed to the orthorhombic structure, the typical Rietveld refinement results are shown in Figure 2c. When the pressure was further increased to 52.2 GPa, several new Bragg peaks

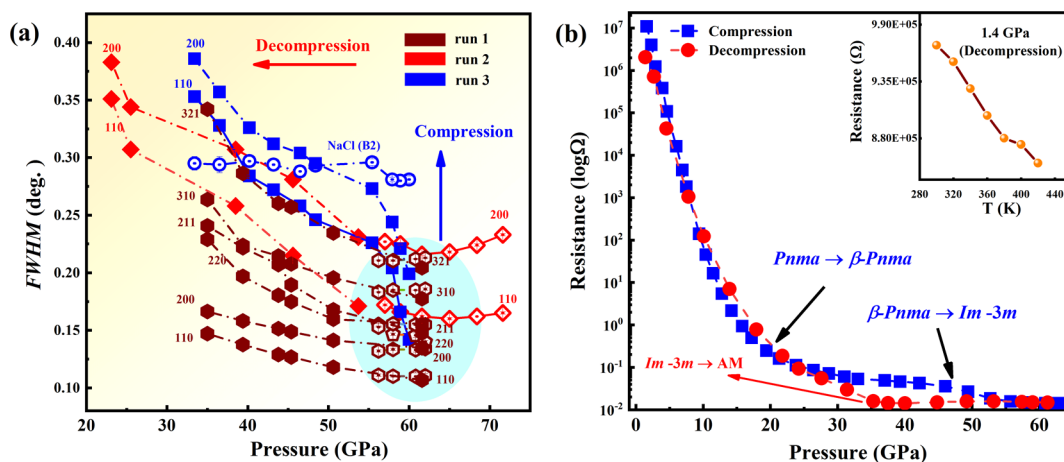


Figure 3. (a) Relationships of the FWHM of the bcc phase of Sb_2Se_3 and NaCl (B2-type) vs pressure during compression and decompression cycles. (b) Pressure dependence of the resistance of Sb_2Se_3 during compression and decompression cycles without PTM, the inset shows the temperature-dependence of the resistance of Sb_2Se_3 at 1.4 GPa in the decompression run.

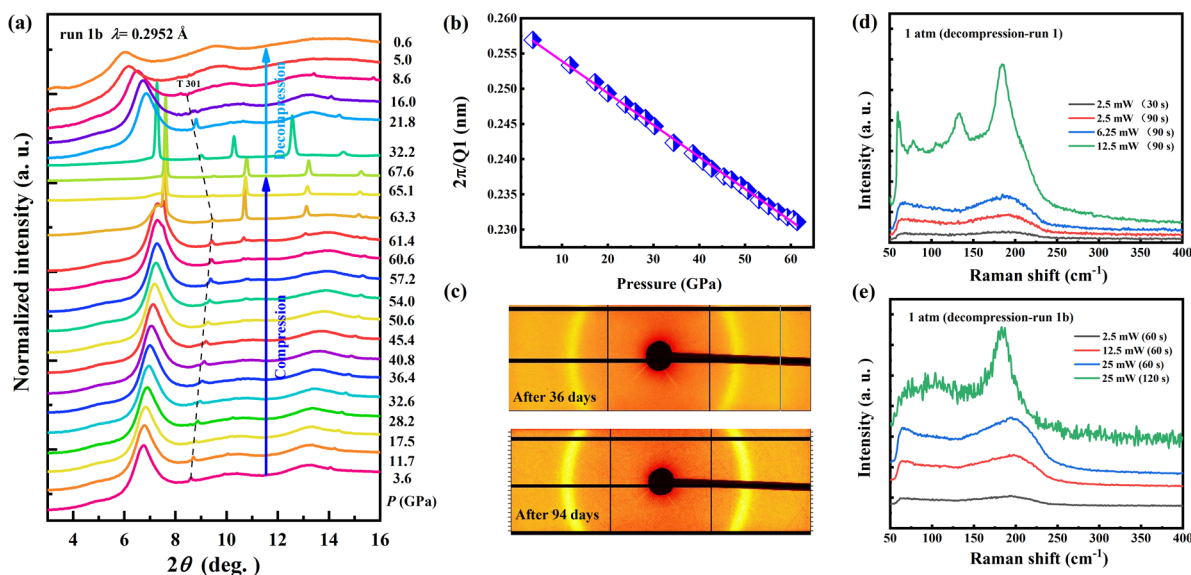


Figure 4. (a) Recompression and decompression of the amorphous Sb_2Se_3 obtained from run 1a with neon as the PTM (marked as run 1b). (b) The inverse main amorphous diffraction peak position $2\pi/Q_1$ of the amorphous Sb_2Se_3 as a function of pressure. (c) The raw 2D XRD patterns of fully released Sb_2Se_3 obtained from run 1b collected at the 4W2 beamline of BSRF after 36 and 94 days. The heating effect of laser on the sample quenched from (d) Raman measurement and (e) run 1b at ambient pressure.

emerged in the XRD pattern and marked with asterisks in Figure 2b, which meant that Sb_2Se_3 began transforming into the site-disordered bcc structure (space group Im-3m). The transition is almost completed at 58.0 GPa, typical Rietveld refinement result is shown in Figure 2d, within the bcc structure, Sb and Se atoms are disordered to randomly share the 2(a) sites, similar to those of Bi_2Te_3 and Sb_2Te_3 . The lattice parameters and volumes derived from Le Bail refinements as a function of pressures in the compression process of run 1a for Sb_2Se_3 are shown in Figure 2e and Figure S2. As can be seen in the inset of Figure S2, the a -axis shows a discontinuous decrease at about 12.4 GPa, and the similar changes have been found in those of b - and c -axes. The results undoubtedly indicate that a structural transition takes place at about 12.4 GPa accompanied 0.77% volume drops, as shown in Figure 2e, which is consistent with our Raman measurements. Here, we can label the new phase as $\beta\text{-Pnma}$.

Unexpectedly, when pressure is lower than about 25.2 GPa (run 1a) in the decompression run, Sb_2Se_3 transforms into an amorphous state (AM) until the ambient pressure, indicated by broad scattering peaks in the XRD pattern, as shown in Figure 2a. To study the effect of nonhydrostatic condition on the structural transitions in the decompression cycle, another independent runs were also performed with the methanol–ethanol (4:1) mixture (run 2) and NaCl as the PTM (run 3), the similar amorphous phase was observed as shown in Figure S2a,b. The pressure dependence of the FWHM of NaCl and the bcc phase over the experimental pressure range is plotted in Figure 3a. Upon pressure release, the FWHM of peaks for the bcc structure of Sb_2Se_3 increases dramatically in all experimental runs, while those of NaCl (B2-type) remain almost unaffected upon decreasing pressure. Furthermore, the effect of pressure on the FWHM of peaks for the bcc phase of Sb_2Se_3 in the compression process (runs 1a and 2) is also displayed in Figure 3a. We can find that the FWHM of the bcc

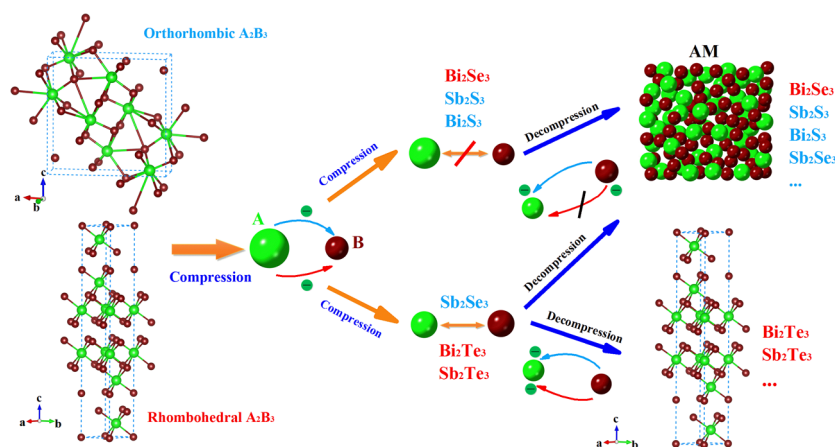


Figure 5. Schematic views of the structural evolutions of A_2B_3 -form ($A = \text{Sb, Bi}$; $B = \text{S, Se, Te}$) compounds during compression and decompression.

phase increased slowly as pressure increased. Generally, pressure-induced Bragg peak broadening occurs in XRD patterns upon compression related to the effects of structural disorder, amorphization, nonhydrostatic conditions, grain size effects, or other structural defects.^{67,68} However, rare studies focus on the phenomenon of Bragg peak broadening in the decompression process. Based on our experimental results, we can attribute the peak broadening of the bcc phase of Sb_2Se_3 to the effect of structural disorder, and the AM phase of Sb_2Se_3 can only be formed by releasing pressure after the transformation to the bcc structure, as shown in Figure S3c,d.

To better understand the relationship between electrical properties and structural phase transitions, the in situ high-pressure electrical resistance measurements of Sb_2Se_3 were performed up to 65 GPa, the pressure dependence of resistance (R - P) is shown in Figure 3b. Upon compression, two inflection points can be observed at 13.5 and 44.6 GPa, respectively. However, in the decompression process, only one inflection point can be found below 35.3 GPa. These inflection points are consistent with the phase transitions observed in the XRD experiments; therefore, the R - P curves of Sb_2Se_3 can reveal the critical pressures of structural phase transitions at high pressure and further verify our experimental results. Furthermore, we can find that the resistivity of AM at ambient conditions is very close to that of the $Pnma$ phase and shows a semiconductor-like conduction, as shown in the inset of Figure 3b.

To give an insight in the behavior of AM and improve our understanding in fundamental relationships between the orthorhombic and AM phases of Sb_2Se_3 , we recompressed the sample obtained from run 1a with neon as PTM (run 1b), the XRD patterns in the compression and decompression process are shown in Figure 4. AM directly transformed into the bcc phase at about 61.4 GPa, which is distinctly higher than the transition pressure during compression of run 1a (52.2 GPa), and the transition is reversible. The reverse main amorphous diffraction peak position $2\pi/Q_1$ correlates with the volume of glass with a power law function, which can be conveniently used to reflect the relative volume (density) change as a function of pressure. Figure 4b shows the inverse main amorphous diffraction peak position $2\pi/Q_1$ of the AM phase of Sb_2Se_3 as a function of pressure, which was estimated from the diffraction peak fitting using a Voigt line profile after subtracting the baseline. No clear change was detected, and

this confirms that polymorphic transitions do not exist in the AM phase of Sb_2Se_3 during compression. Therefore, the AM is more stable than the orthorhombic structure under high pressure. Figure 4c shows the raw 2D XRD patterns of the quenched sample obtained from run 1b after 36 and 94 days, respectively. Obviously, no recrystallization was found, and the AM phase is stable at ambient conditions. To distinguish the Raman character of $Pnma$ and AM of Sb_2Se_3 , we increased the laser power and exposure time, as shown in Figure 4d, we can find that they have very different Raman peaks, and AM phase can directly transform into the original structure at low pressure by laser heating. Surprisingly, the structural stability of amorphous Sb_2Se_3 at high temperature was remarkably enhanced after recompression, even if the laser power was increased to 25 mW, the amorphous Sb_2Se_3 phase has not completely transformed into the $Pnma$ phase, as shown in Figure 4e. Considering the quite low oxidation temperature of orthorhombic Sb_2Se_3 (as shown in Figure S1d), the application of amorphous Sb_2Se_3 may promote the structural stability and improve the performance of these thermoelectric materials.

The crystalline-to-amorphous transition is quite rare when the pressure is released. In previous work, an irreversible structural transition of Bi_2Se_3 was found in the relaxation process,^{57,59} and Sb_2S_3 was also transformed into an amorphous phase under nonhydrostatic condition.⁵⁰ It seems that the pressure conditions have an important effect on the formation of the amorphous phase of A_2B_3 in the decompression cycle. However, based on the results of high-pressure Raman and XRD experiments with different PTMs in the rhombohedral (Bi_2Te_3 and Sb_2Te_3 , as shown in Figure S4) and orthorhombic A_2B_3 (Bi_2S_3 and Sb_2S_3 , the results will be presented in else work), we find that the PTMs have little influence on the results of the structural transitions of A_2B_3 compounds. Here, the differences in atomic electronegativity may account for the irreversible structural transition and the amorphization of A_2B_3 (Bi_2Se_3 , Sb_2Se_3 , Sb_2S_3 , and Bi_2S_3) upon decompression. As shown in Figure 5, upon compression, the charge transfers from A (Bi and Sb) to B (S, Se and Te), which makes the atomic radii of Bi-Te, Sb-Te, and Sb-Se become approximately equal and favorable for the formation of site-disorder bcc (Hume-Rothery rules).^{51-53,61,69} However, due to the significant difference of the atomic radii of Bi (1.60 Å)-S (1.00 Å), Bi-Se (1.15 Å) and Sb (1.45 Å)-S⁷⁰ at ambient conditions make it impossible to equalize the two ionic radii in

A_2B_3 under the effect of external pressure, which may hinder the formation of the substitutional alloy in these compounds, and more details will be discussed in other work. According to the Pauling scale, the electronegativity values of Bi, Sb, Te, Se, and S are 2.02, 2.05, 2.10, 2.55, and 2.58, respectively. When A and B atoms have similar electronegativity values, with decreasing pressure from the site-disordered or structural-disordered state, the charges which were transferred from A to B should be returned to the original state and show reversible structural transitions, such as Bi_2Te_3 and Sb_2Te_3 . However, when the electronegativity value of B is far larger than that of A, part of the transferred charges will be “captured” around B even though pressure is fully released, which is favorable to the formation of amorphous phase, such as Sb_2Se_3 , Sb_2S_3 , Bi_2S_3 , and Bi_2Se_3 . Also, these amorphous phases will most likely transform into ordered crystalline structures upon sufficient heating, as shown in Figure 4d. Based on these results, we may offer a novel method to prepare the amorphous materials in which the elements should have a significant difference in the electronegativity values within the compounds, and the amorphous samples can be retained with quenching from high pressure.

CONCLUSIONS

In summary, pressure-induced isostructural and site-disordered transformations were observed in Sb_2Se_3 in the compression process. With decreasing pressure, an amorphous state appeared in Sb_2Se_3 , the differences in atomic electronegativity may be explained for the irreversible transition. More importantly, the structural stability of Sb_2Se_3 will be significantly enhanced at high pressure and temperature. These findings will help to improve understanding of the behavior of A_2B_3 under high pressure and also provide a novel way to search for alloys and amorphous materials.

ASSOCIATED CONTENT

Supporting Information

The Supporting Information is available free of charge at <https://pubs.acs.org/doi/10.1021/acs.jpcc.9b11520>.

Raman spectra of powder Sb_2Se_3 measured at ambient conditions with different powers of the incident laser and exposure times and thermogravimetric analysis (TGA) of Sb_2Se_3 in an air atmosphere; the pressure dependence of lattice parameters for the three phases of Sb_2Se_3 ; the XRD spectra of Sb_2Se_3 plotted against pressure during decompression in run 2 and run 3, and the compression and decompression of Sb_2Se_3 with the methanol–ethanol (4:1) mixture as the PTM up to 45.2 and 55.8 GPa; and the XRD and Raman spectra of Bi_2Te_3 and Sb_2Te_3 versus pressure during compression and decompression at room temperature without PTM (PDF)

AUTHOR INFORMATION

Corresponding Authors

Chuanlong Lin – Center for High Pressure Science and Technology Advanced Research (HPSTAR), Beijing 100094, China; Email: chuanlong.lin@hpstar.ac.cn

Shanmin Wang – Department of Physics, Southern University of Science and Technology, Shenzhen 518055, China;

orcid.org/0000-0001-7273-2786; Email: wangsm@sustech.edu.cn

Yanchun Li – Multidiscipline Research Center, Institute of High Energy Physics, Chinese Academy of Science, Beijing 100049, China; Email: lyc@ihep.ac.cn

Authors

Hu Cheng – Multidiscipline Research Center, Institute of High Energy Physics, Chinese Academy of Science, Beijing 100049, China; Department of Physics, Southern University of Science and Technology, Shenzhen 518055, China; Department of Physics, Wuhan University, Wuhan 430072, China; orcid.org/0000-0003-3526-2097

Junran Zhang – Multidiscipline Research Center, Institute of High Energy Physics, Chinese Academy of Science, Beijing 100049, China; University of Chinese Academy of Sciences, Beijing 100049, China

Pengfei Yu – State Key Laboratory of Metastable Materials Science and Technology, Yanshan University, Qinhuangdao 066004, China

Chao Gu – Department of Physics, Southern University of Science and Technology, Shenzhen 518055, China

Xiangting Ren – Department of Physics, Southern University of Science and Technology, Shenzhen 518055, China; Department of Physics, Wuhan University, Wuhan 430072, China

Xiaodong Li – Multidiscipline Research Center, Institute of High Energy Physics, Chinese Academy of Science, Beijing 100049, China; orcid.org/0000-0002-2290-1198

Yusheng Zhao – Department of Physics, Southern University of Science and Technology, Shenzhen 518055, China

Complete contact information is available at: <https://pubs.acs.org/10.1021/acs.jpcc.9b11520>

Author Contributions

^vH.C. and J.Z. contributed equally.

Notes

The authors declare no competing financial interest.

ACKNOWLEDGMENTS

This work was supported by the National Natural Science Foundation of China (grant no. 11474280), China Postdoctoral Science Foundation (grant no. 2019M652684), the Key Research Platforms and Research Projects of Universities in Guangdong Province (grant no. 2018KZDXM062), the Guangdong Innovative and Entrepreneurial Research Team Program (grant no. 2016ZT06C279), and the Shenzhen Peacock Plan (grant no. KQTD2016053019134356).

REFERENCES

- (1) Buckel, W.; Hilsch, R. Einfluß der Kondensation bei tiefen Temperaturen auf den Elektrischen Widerstand und die Supraleitung für Verschiedene Metalle. *Zeitschrift für Physik* **1954**, *138*, 109–120.
- (2) Buckel, W. Elektronenbeugungs-Aufnahmen von dünnen Metallschichten bei tiefen Temperaturen. *Zeitschrift für Physik* **1954**, *138*, 136–150.
- (3) Jun, W. K.; Willens, R. H.; Duwez, P. Non-Crystalline Structure in Solidified Gold–Silicon Alloys. *Nature* **1960**, *187*, 869.
- (4) Oesterreicher, H.; Clinton, J.; Bittner, H. Hydrides of La-Ni Compounds. *Mater. Res. Bull.* **1976**, *11*, 1241–1247.
- (5) Van Diepen, A. M.; Buschow, K. H. J. Hydrogen Absorption in $CeFe_2$ and $ThFe_3$. *Solid State Commun.* **1977**, *22*, 113–115.
- (6) Yeh, X. L.; Samwer, K.; Johnson, W. L. Formation of an Amorphous Metallic Hydride by Reaction of Hydrogen with Crystalline Intermetallic Compounds—a New Method of Synthesizing Metallic Glasses. *Appl. Phys. Lett.* **1983**, *42*, 242–243.

- (7) Koch, C. C.; Cavin, O. B.; McKamey, C. G.; Scarbrough, J. Preparation of "Amorphous" $\text{Ni}_{60}\text{Nb}_{40}$ by Mechanical Alloying. *Appl. Phys. Lett.* **1983**, *43*, 1017–1019.
- (8) Schwarz, R. B.; Petrich, R. R.; Saw, C. K. The Synthesis of Amorphous Ni-Ti Alloy Powders by Mechanical Alloying. *J. Non-Cryst. Solids* **1985**, *76*, 281–302.
- (9) Schwarz, R. B.; Johnson, W. L. Remarks on Solid State Amorphizing Transformations. *J. Alloy. Compd.* **1988**, *140*, 1–6.
- (10) Thompson, M. O.; Galvin, G. J.; Mayer, J. W.; Peercy, P. S.; Poate, J. M.; Jacobson, D. C.; Cullis, A. G.; Chew, N. G. Melting Temperature and Explosive Crystallization of Amorphous Silicon during Pulsed Laser Irradiation. *Phys. Rev. Lett.* **1984**, *52*, 2360.
- (11) Goncharov, A. F.; Makarenko, I. N.; Stishov, S. M. Graphite at Pressures up to 55 GPa: Optical Properties and Raman Scattering—Amorphous Carbon. *Sov. Phys. JETP* **1989**, *69*, 380–381.
- (12) Goncharov, A. F. Observation of Amorphous Phase of Carbon at Pressures Above 23 GPa. *ZhETF Pis ma Redaktsiiu* **1990**, *51*, 368.
- (13) Clarke, D. R.; Kroll, M. C.; Kirchner, P. D.; Cook, R. F.; Hockey, B. J. Amorphization and Conductivity of Silicon and Germanium Induced by Indentation. *Phys. Rev. Lett.* **1988**, *60*, 2156.
- (14) Deb, S. K.; Wilding, M.; Somayazulu, M.; McMillan, P. F. Pressure-Induced Amorphization and an Amorphous–Amorphous Transition in Densified Porous Silicon. *Nature* **2001**, *414*, 528.
- (15) Imai, M.; Mitamura, T.; Yaoita, K.; Tsuji, K. Pressure-Induced Phase Transition of Crystalline and Amorphous Silicon and Germanium at Low Temperatures. *High Pressure Res.* **1996**, *15*, 167–189.
- (16) Mishima, O.; Calvert, L. D.; Whalley, E. 'Melting Ice' I at 77 K and 10 kbar: A New Method of Making Amorphous Solids. *Nature* **1984**, *310*, 393.
- (17) Mishima, O.; Calvert, L. D.; Whalley, E. An Apparently First-Order Transition Between Two Amorphous Phases of Ice Induced by Pressure. *Nature* **1985**, *314*, 76.
- (18) Bell, P. M.; Roseboom, E., Jr. Melting Relationships of Jadeite and Albite to 45 kilobars with Comments on Melting Diagrams of Binary Systems at High Pressures. *Mineral. Soc. Amer. Spec. Pap.* **1969**, *2*, 151–169.
- (19) Williams, D. W.; Kennedy, G. C. The Melting of Jadeite to 60 Kilobars. *Am. J. Sci.* **1970**, *269*, 481–488.
- (20) Li, Q.; Li, S.; Wang, K.; Li, X.; Liu, J.; Liu, B.; Zou, G.; Zou, B. Pressure-Induced Isosymmetric Phase Transition in Sulfamic Acid: A Combined Raman and X-Ray Diffraction Study. *J. Chem. Phys.* **2013**, *138*, 214505.
- (21) Lü, X.; Wang, Y.; Stoumpos, C. C.; Hu, Q.; Guo, X.; Chen, H.; Yang, L.; Smith, J. S.; Yang, W.; Zhao, Y.; et al. Enhanced Structural Stability and Photo Responsiveness of $\text{CH}_3\text{NH}_3\text{SnI}_3$ Perovskite via Pressure-Induced Amorphization and Recrystallization. *Adv. Mater.* **2016**, *28*, 8663–8668.
- (22) Wang, Z.; Schliehe, C.; Wang, T.; Nagaoka, Y.; Cao, Y. C.; Bassett, W. A.; Wu, H.; Fan, H.; Weller, H. Deviatoric Stress Driven Formation of Large Single-Crystal PbS Nanosheet from Nanoparticles and in situ Monitoring of Oriented Attachment. *J. Am. Chem. Soc.* **2011**, *133*, 14484–14487.
- (23) Belash, I. T.; Ponyatovskii, E. G. Phase Diagram of CdSb Semiconductive Compound to 80 Kbar. *High Temp. - High Pressures* **1974**, *8*, 24–191.
- (24) Ponyatovsky, E. G.; Barkalov, O. I. Pressure-Induced Amorphous Phases. *Mater. Sci. Rep.* **1992**, *8*, 147–191.
- (25) Yvon, P. J.; Schwarz, R. B.; Schiferl, D.; Johnson, W. L. Covalent and Liquid-Like Amorphous Phases in Al[Sbnd]Ge Alloys. *Phil. Mag. Lett.* **1995**, *72*, 167–174.
- (26) Snyder, G. J.; Toberer, E. S. Complex Thermoelectric Materials. In *Materials for Sustainable Energy: A Collection of Peer-Reviewed Research and Review Articles from Nature Publishing Group*; World Scientific: 2011; pp 101–110.
- (27) Moon, S. J.; Itzhaik, Y.; Yum, J. H.; Zakeeruddin, S. M.; Hodes, G.; Grätzel, M. Sb_2S_3 -Based Mesoscopic Solar Cell Using an Organic Hole Conductor. *J. Phys. Chem. Lett.* **2010**, *1*, 1524–1527.
- (28) Jayakumar, S.; Balasubramanian, C.; Narayandass, S. K.; Mangalaraj, D.; Vallabhan, C. P. G. Optical Recording Characteristics of Sb_2Se_3 Thin Films using a CW-Ar+ Laser. *Thin Solid Films* **1995**, *266*, 62–68.
- (29) Ma, J.; Wang, Y.; Wang, Y.; Chen, Q.; Lian, J.; Zheng, W. Controlled Synthesis of One-Dimensional Sb_2Se_3 Nanostructures and Their Electrochemical Properties. *J. Phys. Chem. C* **2009**, *113*, 13588–13592.
- (30) Chen, Y. L.; Analytis, J. G.; Chu, J. H.; Liu, Z. K.; Mo, S. K.; Qi, X. L.; Zhang, H. J.; Lu, D. H.; Dai, X.; Fang, Z.; et al. Experimental Realization of a Three-Dimensional Topological Insulator, Bi_2Te_3 . *Science* **2009**, *325*, 178–181.
- (31) Zhang, H.; Liu, C.-X.; Qi, X.-L.; Dai, X.; Fang, Z.; Zhang, S.-C. Topological Insulators in Bi_2Se_3 , Bi_2Te_3 and Sb_2Te_3 with a Single Dirac Cone on the Surface. *Nat. Phys.* **2009**, *5*, 438.
- (32) Badding, J. V.; Meng, J. F.; Polvani, D. A. Pressure Tuning in the Search for New and Improved Solid State Materials. *Chem. Mater.* **1998**, *10*, 2889–2894.
- (33) Ovsyannikov, S. V.; Grigor'eva, Y. A.; Vorontsov, G. V.; Luk'yanova, L. N.; Kutasov, V. A.; Shchennikov, V. V. Thermoelectric Properties of $p\text{-Bi}_{2-x}\text{Sb}_x\text{Te}_3$ Solid Solutions Under Pressure. *Phys. Solid State* **2012**, *54*, 261–266.
- (34) Ovsyannikov, S. V.; Shchennikov, V. V.; Vorontsov, G. V.; Manakov, A. Y.; Likhacheva, A. Y.; Kulbachinskii, V. A. Giant Improvement of Thermoelectric Power Factor of Bi_2Te_3 Under Pressure. *J. Appl. Phys.* **2008**, *104*, No. 053713.
- (35) Polvani, D. A.; Meng, J. F.; Shekar, N. V. C.; Sharp, J.; Badding, J. V. Large Improvement in Thermoelectric Properties in Pressure-Tuned $p\text{-Type Sb}_{1.3}\text{Bi}_{0.5}\text{Te}_3$. *Chem. Mater.* **2001**, *13*, 2068–2071.
- (36) Gomis, O.; Vilaplana, R.; Manjón, F. J.; Rodríguez-Hernández, P.; Pérez-González, E.; Muñoz, A.; Kucek, V.; Drasar, C. Lattice Dynamics of Sb_2Te_3 at High Pressures. *Phys. Rev. B* **2011**, *84*, 174305.
- (37) Polian, A.; Gauthier, M.; Souza, S. M.; Trichês, D. M.; de Lima, J. C.; Grandi, T. A. Two-Dimensional Pressure-Induced Electronic Topological Transition in Bi_2Te_3 . *Phys. Rev. B* **2011**, *83*, 113106.
- (38) Vilaplana, R.; Gomis, O.; Manjón, F. J.; Segura, A.; Pérez-González, E.; Rodríguez-Hernández, P.; Muñoz, A.; González, J.; Marín-Borrás, V.; Muñoz-Sanjosé, V.; et al. High-Pressure Vibrational and Optical Study of Bi_2Te_3 . *Phys. Rev. B* **2011**, *84*, 104112.
- (39) Vilaplana, R.; Santamaría-Pérez, D.; Gomis, O.; Manjón, F. J.; González, J.; Segura, A.; Muñoz, A.; Rodríguez-Hernández, P.; Pérez-González, E.; Marín-Borrás, V.; Muñoz-Sanjosé, V.; Drasar, C.; Kucek, V. Structural and Vibrational Study of Bi_2Se_3 Under High Pressure. *Phys. Rev. B* **2011**, *84*, 184110.
- (40) Efthimiopoulos, I.; Kemichick, J.; Zhou, X.; Khare, S. V.; Ikuta, D.; Wang, Y. High-Pressure Studies of Bi_2S_3 . *J. Phys. Chem. A* **2014**, *118*, 1713–1720.
- (41) Einaga, M.; Tanabe, Y.; Nakayama, A.; Ohmura, A.; Ishikawa, F.; Yamada, Y. New Superconducting Phase of Bi_2Te_3 Under Pressure Above 11 GPa. *J. Phys.: Conf. Ser.* **2010**, *215*, No. 012036.
- (42) Hor, Y. S.; Williams, A. J.; Checkelsky, J. G.; Roushan, P.; Seo, J.; Xu, Q.; Zandbergen, H. W.; Yazdani, A.; Ong, N. P.; Cava, R. J. Superconductivity in $\text{Cu}_x\text{Bi}_2\text{Se}_3$ and Its Implications for Pairing in the Undoped Topological Insulator. *Phys. Rev. Lett.* **2010**, *104*, No. 057001.
- (43) Sasaki, S.; Kriener, M.; Segawa, K.; Yada, K.; Tanaka, Y.; Sato, M.; Ando, Y. Topological Superconductivity in $\text{Cu}_x\text{Bi}_2\text{Se}_3$. *Phys. Rev. Lett.* **2011**, *107*, 217001.
- (44) Zhang, C.; Sun, L.; Chen, Z.; Zhou, X.; Wu, Q.; Yi, W.; Guo, J.; Dong, X.; Zhao, Z. Phase Diagram of a Pressure-Induced Superconducting State and Its Relation to the Hall Coefficient of Bi_2Te_3 Single Crystals. *Phys. Rev. B* **2011**, *83*, 140504.
- (45) Zhang, J. L.; Zhang, S. J.; Weng, H. M.; Zhang, W.; Yang, L. X.; Liu, Q. Q.; Feng, S. M.; Wang, X. C.; Yu, R. C.; Cao, L. Z.; et al. Pressure-Induced Superconductivity in Topological Parent Compound Bi_2Te_3 . *Proc. Natl. Acad. Sci. U. S. A.* **2011**, *108*, 24–28.
- (46) Kong, P. P.; Zhang, J. L.; Zhang, S. J.; Zhu, J.; Liu, Q. Q.; Yu, R. C.; Fang, Z.; Jin, C. Q.; Yang, W. G.; Yu, X. H.; Zhu, J. L.; Zhao, Y. S.

Superconductivity of the Topological Insulator Bi_2Se_3 at High Pressure. *J. Phys.: Condens. Matter* **2013**, *25*, 362204.

(47) Zhu, J.; Zhang, J. L.; Kong, P. P.; Zhang, S. J.; Yu, X. H.; Zhu, J. L.; Liu, Q. Q.; Li, X.; Yu, R. C.; Ahuja, R.; et al. Superconductivity in Topological Insulator Sb_2Te_3 Induced by Pressure. *Sci. Rep.* **2013**, *3*, 2016.

(48) Kong, P. P.; Sun, F.; Xing, L. Y.; Zhu, J.; Zhang, S. J.; Li, W. M.; Liu, Q. Q.; Wang, X. C.; Feng, S. M.; Yu, X. H.; et al. Superconductivity in Strong Spin Orbital Coupling Compound Sb_2Se_3 . *Sci. Rep.* **2014**, *4*, 6679.

(49) Zhang, J.; Han, Y.; Liu, C.; Zhang, X.; Ke, F.; Peng, G.; Ma, Y.; Ma, Y.; Gao, C. Semiconductor-to-Metal Transition of Bi_2Se_3 Under High Pressure. *Appl. Phys. Lett.* **2014**, *105*, No. 062102.

(50) Dai, L.; Liu, K.; Li, H.; Wu, L.; Hu, H.; Zhuang, Y.; Yang, L.; Pu, C.; Liu, P. Pressure-Induced Irreversible Metallization Accompanying the Phase Transitions in Sb_2S_3 . *Phys. Rev. B* **2018**, *97*, No. 024103.

(51) Einaga, M.; Ohmura, A.; Nakayama, A.; Ishikawa, F.; Yamada, Y.; Nakano, S. Pressure-Induced Phase Transition of Bi_2Te_3 to a bcc Structure. *Phys. Rev. B* **2011**, *83*, No. 092102.

(52) Zhao, J.; Liu, H.; Ehm, L.; Chen, Z.; Sinogeikin, S.; Zhao, Y.; Gu, G. Pressure-Induced Disordered Substitution Alloy in Sb_2Te_3 . *Inorg. Chem.* **2011**, *50*, 11291–11293.

(53) Zhu, L.; Wang, H.; Wang, Y.; Lv, J.; Ma, Y.; Cui, Q.; Ma, Y.; Zou, G. Substitutional Alloy of Bi and Te at High Pressure. *Phys. Rev. Lett.* **2011**, *106*, 145501.

(54) Ma, Y.; Liu, G.; Zhu, P.; Wang, H.; Wang, X.; Cui, Q.; Liu, J.; Ma, Y. Determinations of the High-Pressure Crystal Structures of Sb_2Te_3 . *J. Phys.: Condens. Matter* **2012**, *24*, 475403.

(55) Souza, S. M.; Poffo, C. M.; Trichês, D. M.; De Lima, J. C.; Grandi, T. A.; Polian, A.; Gauthier, M. High Pressure Monoclinic Phases of Sb_2Te_3 . *Phys. B* **2012**, *407*, 3781–3789.

(56) Liu, G.; Zhu, L.; Ma, Y.; Lin, C.; Liu, J.; Ma, Y. Stabilization of 9/10-Fold Structure in Bismuth Selenide at High Pressures. *J. Phys. Chem. C* **2013**, *117*, 10045–10050.

(57) Zhao, J.; Liu, H.; Ehm, L.; Dong, D.; Chen, Z.; Gu, G. High-Pressure Phase Transitions, Amorphization, and Crystallization Behaviors in Bi_2Se_3 . *J. Phys.: Condens. Matter* **2013**, *25*, 125602.

(58) Yu, Z.; Wang, L.; Hu, Q.; Zhao, J.; Yan, S.; Yang, K.; Sinogeikin, S.; Gu, G.; Mao, H.-K. Structural Phase Transitions in Bi_2Se_3 Under High Pressure. *Sci. Rep.* **2015**, *5*, 15939.

(59) Cheng, H.; Zhang, J.; Li, Y.; Li, G.; Li, X. Structure Determination of the High-Pressure Phases of Topological Insulator Bi_2Se_3 Using Experiments and Calculations. *J. Appl. Phys.* **2017**, *121*, 225902.

(60) Efthimiopoulos, I.; Buchan, C.; Wang, Y. Structural Properties of Sb_2S_3 Under Pressure: Evidence of an Electronic Topological Transition. *Sci. Rep.* **2016**, *6*, 24246.

(61) Efthimiopoulos, I.; Zhang, J.; Kucway, M.; Park, C.; Ewing, R. C.; Wang, Y. Sb_2Se_3 Under Pressure. *Sci. Rep.* **2013**, *3*, 2665.

(62) Mao, H. K.; Xu, J.; Bell, P. M. Calibration of the Ruby Pressure Gauge to 800 kbar Under Quasi-Hydrostatic Conditions. *J. Geophys. Res.: Solid Earth* **1986**, *91*, 4673–4676.

(63) Hammersley, J. *Fit2d User Manual*; ESRF: Grenoble, France, 1996.

(64) Toby, B. H. EXPGUI, a Graphical User Interface for GSAS. *J. Appl. Crystallogr.* **2001**, *34*, 210–213.

(65) Bera, A.; Pal, K.; Muthu, D. V. S.; Sen, S.; Guptasarma, P.; Waghmare, U. V.; Sood, A. K. Sharp Raman Anomalies and Broken Adiabaticity at a Pressure Induced Transition from Band to Topological Insulator in Sb_2Se_3 . *Phys. Rev. Lett.* **2013**, *110*, 107401.

(66) Shongalova, A.; Correia, M. R.; Vermang, B.; Cunha, J. M. V.; Salomé, P. M. P.; Fernandes, P. A. On the Identification of Sb_2Se_3 Using Raman Scattering. *MRS Commun.* **2018**, *8*, 865–870.

(67) Gerward, L.; Mo/rup, S.; Topso/e, H. Particle Size and Strain Broadening in Energy-Dispersive X-Ray Powder Patterns. *J. Appl. Phys.* **1976**, *47*, 822–825.

(68) Sharma, S. M.; Sikka, S. K. Pressure Induced Amorphization of Materials. *Prog. Mater. Sci.* **1996**, *40*, 1–77.

(69) Hume-Rothery, W. The Structure of Metals and Alloys. *Indian J. Phys.* **1969**, *11*, 74.

(70) Slater, J. C. Atomic Radii in Crystals. *J. Chem. Phys.* **1964**, *41*, 3199–3204.

(71) Birch, F. Finite Elastic Strain of Cubic Crystals. *Phys. Rev.* **1947**, *71*, 809.